

Article

Noble Metal Modified TiO₂ Hierarchically Structured Microspheres with Enhanced Photocatalytic Activity

Haisheng Huang^{1,2}, Juan Wang^{1,2,3}, Qi Kong^{1,2}, Yao Xu^{1,2}, Zhishun Wei^{1,2,3,*}  and Ying Chang^{1,2,3,*}

¹ Hubei Provincial Key Laboratory of Green Materials for Light Industry, New Materials and Green Manufacturing Talent Introduction and Innovation Demonstration Base, Hubei University of Technology, Wuhan 430068, China; hhsheng98@outlook.com (H.H.); jwang@hbut.edu.cn (J.W.); kongqi1219@outlook.com (Q.K.); 102100433@hbut.edu.cn (Y.X.)

² School of Materials and Chemical Engineering, Hubei University of Technology, Wuhan 430068, China

³ Hubei Longzhong Laboratory, Xiangyang 441000, China

* Correspondence: wei.zhishun@hbut.edu.cn (Z.W.); cy0025@hbut.edu.cn (Y.C.)

Abstract: Anatase TiO₂ hierarchically structured microspheres with co-exposed {001}/{101} facets were prepared by a facile one-pot hydrothermal method. The influences of reaction temperature on the morphology and crystallization of microspheres were investigated systematically. The obtained microspheres possessed better morphology and crystallization when the reaction temperature was 160 °C. Different noble metals (Au, Ag, Cu, Pt, Pd) were used for the microspheres modification, and the experimental results exhibited that the photocatalytic activities of the noble metal modified microspheres were enhanced obviously, especially for the Pt-modified sample (TPt), which showed the highest photocatalytic activity in degradation of tetracycline hydrochloride (the TPt sample showed the largest improvement, i.e., the activity reached 1.47 times higher than that of the bare sample) and hydrogen production (the largest improvement was also observed for the TPt sample, i.e., the activity was more than 30 times as the bare sample, reaching more than 300 μmol·g⁻¹·h⁻¹). Finally, a photocatalytic reaction mechanism involving the synergy of co-exposed {001}/{101} crystal facets with noble metals was proposed according to the as-obtained experimental results.

Keywords: titanium oxide; microsphere; hierarchical structure; noble metal; photocatalysis



Citation: Huang, H.; Wang, J.; Kong, Q.; Xu, Y.; Wei, Z.; Chang, Y. Noble Metal Modified TiO₂ Hierarchically Structured Microspheres with Enhanced Photocatalytic Activity. *Catalysts* **2023**, *13*, 995. <https://doi.org/10.3390/catal13060995>

Academic Editor: Weilin Dai

Received: 11 May 2023

Revised: 8 June 2023

Accepted: 9 June 2023

Published: 12 June 2023



Copyright: © 2023 by the authors. Licensee MDPI, Basel, Switzerland. This article is an open access article distributed under the terms and conditions of the Creative Commons Attribution (CC BY) license (<https://creativecommons.org/licenses/by/4.0/>).

1. Introduction

Photocatalysis is a promising technology that could efficiently solve current energy and environmental challenges. Although the development of many non-TiO₂ photocatalytic materials has further expanded the application range of photocatalysis [1–3], TiO₂ still has broad application potential due to its unique advantages, such as high photostability, superior redox ability, low price, and environment-friendly. As the most widely studied photocatalyst, anatase TiO₂ with various sizes and morphology is used in the fields of energy and environmental application. For example, nanosized TiO₂ powder usually can exhibit high photocatalytic activity for its large specific surface area, whereas it is hard to separate and reuse from the aqueous suspensions for its tiny size. Meanwhile, micro-sized TiO₂ powder is a good candidate for solving the recycling problem due to its relatively large size; however, its low photocatalytic activity limits its practical application. Therefore, a micron-scale TiO₂ that is hierarchically structured and consisting of quasi-nanoparticles has attracted a lot of attention because of its large size and unique surface morphology [4–7]. Among them, TiO₂ hierarchically structured microsphere has more advantages for its excellent monodispersion, and it has been confirmed that the photocatalytic performance of the TiO₂ microsphere mainly depends on the crystal facet characteristics of its structural units. In order to enhance the photocatalytic performance, turning the structural units into octahedrals or decahedrons by

crystal facet tailoring is a good strategy to improve the intrinsic photocatalytic performance of TiO_2 , which is exposing the {001} and {101} facets. In contrast to {101} facets with only 50% five-fold coordinate unsaturated Ti (Ti 5c) atoms acting as reactive sites in heterogeneous reactions, {001} facets with 100% Ti 5c atoms are considered more reactive and have a higher photocatalytic performance than that of {101} facets for its more active sites [7]. Then, the TiO_2 anatase crystals with a high {001} facet exposure ratio from 47% to 89% [8] up to nearly 100% [9] are reported. However, the co-existence of {001} and {101} facets of anatase TiO_2 to form a “surface heterojunction” is beneficial to enhance its intrinsic photocatalytic performance and was proposed by Yu [10] et al. in recent years. In addition, other effective strategies were also employed for improving the photocatalytic performance of TiO_2 , such as ion doping [11–16], semiconductor coupling [17–21], noble metal deposition [22–26], etc.

Herein, we focus on improving the photocatalytic performance of TiO_2 microspheres through a combined strategy by exposing its {001}/ {101} facets and depositing the noble metals. TiO_2 hierarchically structured microspheres with co-exposed {001} and {101} facets were synthesized by the one-pot hydrothermal method. The experimental results of the decolorization of tetracycline hydrochloride (TC) aqueous solution and photocatalytic hydrogen generation confirmed that the modified samples showed a significantly enhanced photocatalytic performance. The co-exposed {101}/ {001} crystal facets and noble metal modification synergistically enhanced the separation of the photogenerated electron-hole pairs. Finally, a photocatalytic mechanism was proposed.

2. Results and Discussion

2.1. Structures and Morphology

The XRD patterns of the samples prepared at different reaction temperatures are shown in Figure 1. All diffraction peaks were well indexed to the anatase structure of TiO_2 (PDF 01-084-1825). The sharp diffraction patterns indicated all the samples were well-crystallized anatase TiO_2 powders, and Raman spectroscopy also confirmed that these samples were composed of anatase phase TiO_2 , which was consistent with XRD analysis (Figure S1). With the increase in reaction temperature, the intensity and width of the anatase peaks were gradually changed to be stronger and narrower, respectively. Besides, with the further increase of the reaction temperature from 160 to 200 °C, the crystallinity of the sample was not increased obviously, which indicated that the reaction temperature had an important influence on the crystalline phase and a suitable reaction temperature (e.g., 160 °C) was beneficial to forming a well-crystallized anatase phase.

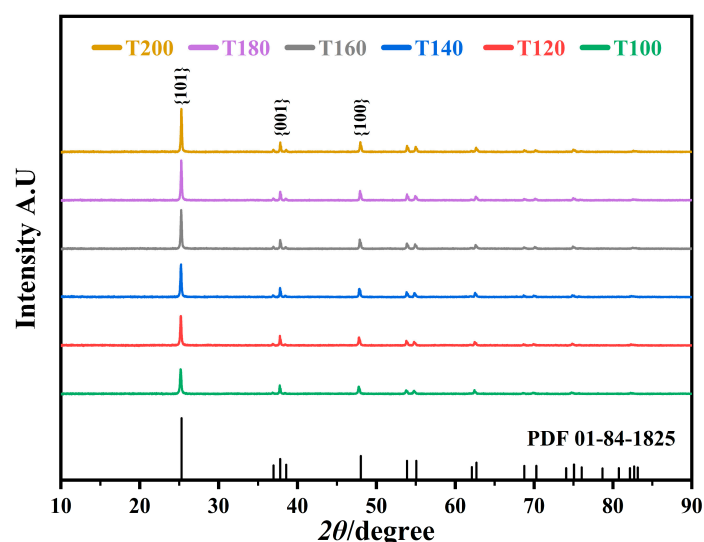


Figure 1. XRD patterns of samples prepared at different reaction temperatures denoted as T100, T120, T140, T160, T180, and T200, respectively.

The SEM images of the samples prepared at 100, 120, 140, 160, 180, and 200 °C are shown in Figure 2. The results indicate that the reaction temperature significantly influenced the surface morphology and size of the as-synthesized powder samples. When the reaction temperature was 100 °C, as shown in Figure 2a,b, the samples were flower-like microspheres with a rough surface, and no clear exposed crystal facets could be found. As the reaction temperature increased to 120 °C, clear exposed crystal facets appeared on the surface of flower-like microspheres, but there were still many surface defects. With a further increase of the reaction temperature to 140 °C, the crystal facets on the surface of the microspheres were clearer, and the defects were reduced. When the reaction temperature increased to 160 °C, the microspheres showed a good hierarchical structure with clear and complete crystal facets and fewer defects, indicating that the reaction temperature increase could efficiently promote the formation of crystal facets and microspheres. However, when the reaction temperature was increased to 180 °C, the boundaries of crystal facets became unclear again, and a large number of holes appeared on the surface of the microspheres. Similarly, when further increasing the reaction temperature to 200 °C, the number of surface defects and holes on the microspheres also increased accordingly, indicating that an excessively high reaction temperature was unsuitable for forming microspheres with clear crystal facets and fewer defects. According to the dissolution–deposition mechanism, the excessively high reaction temperature would accelerate the dissolution–recrystallization rate and the etching effect of the F ions, resulting in the increase of surface defects and the appearance of incomplete crystal facets [27,28]. Furthermore, with the increase of the reaction temperature, the particle size of the microspheres was also increased slightly (Table S1).

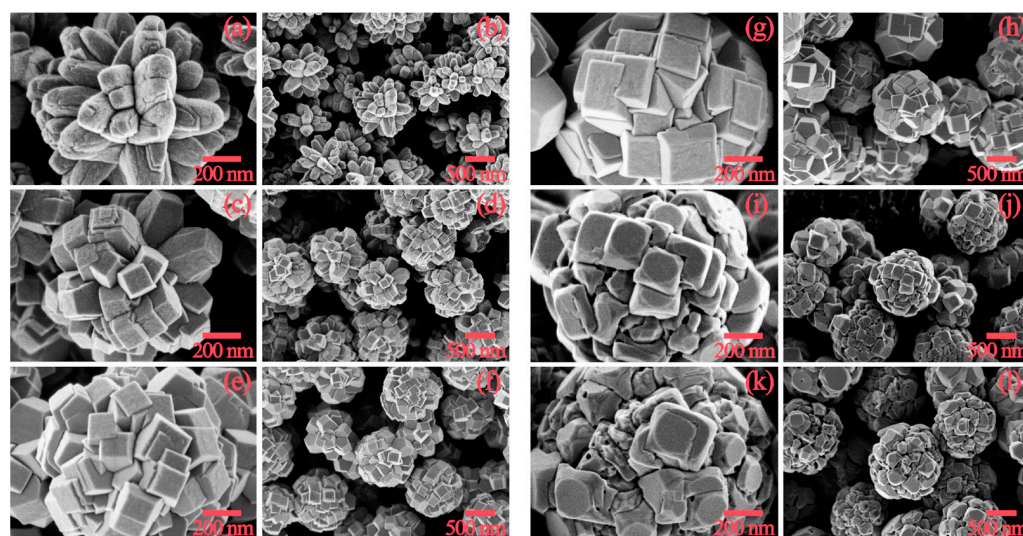


Figure 2. SEM images of samples prepared at different reaction temperatures (°C): (a,b) 100; (c,d) 120; (e,f) 140; (g,h) 160; (i,j) 180 and (k,l) 200.

In order to study the T160 sample in more detail, the particle size distribution of the T160 was checked. As shown in Figure 3, the laser particle size measurement revealed that the T160 sample had a narrow size distribution and a consistent particle size with domain sizes in the range from 0.5 to 2 μm ; more than 90% of the microspheres were smaller than 2 μm . Meanwhile, Table 1 shows the particle size range, average particle size, and volume fraction of the T160 sample. It can be seen in the Table that the average particle size of T160 is about 1.1 μm , which was consistent with those obtained from the SEM images (Figures 2 and S2). As demonstrated in the XRD patterns (Figure 1) and SEM images (Figure 2), all the samples have a hierarchical structure consisting of quasi-nanosized TiO_2 anatase particles, providing a highly interconnected mesoporous structure. This is

also verified by the N₂ adsorption–desorption isotherm of the sample T160 (as shown in Figure 4). The isotherm of T160 was a typical IV-type curve in the relative pressure range of 0.45 to 1.0, and the hysteresis loop was H3-type, which reflects the characteristics of mesoporous materials with slits [29]. The pore size distribution curves showed that the pore size was mostly about 20 nm, and the specific surface area was 5.36 m²/g according to the calculation from nitrogen adsorption–desorption isotherms; these were also consistent with the results based on the SEM images.

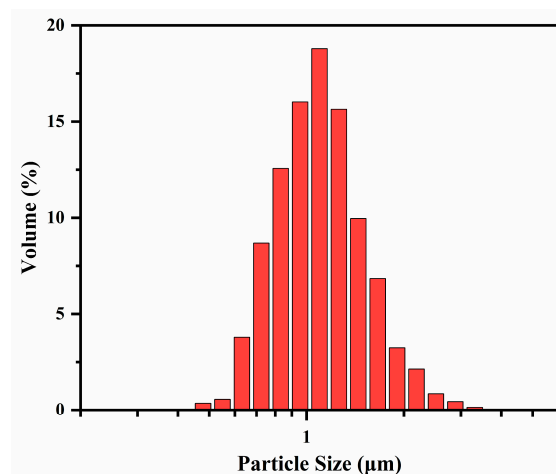


Figure 3. Particle size distribution of the T160 sample.

Table 1. Average particle size, particle size range, and volume fraction of sample.

Volume (%)	50.45	81.65	92.28	100
Particle size range (μm)	0.96–1.26	0.73–1.45	0.63–1.66	0.48–3.31
Average particle size (μm)	1.11	1.07	1.09	1.16

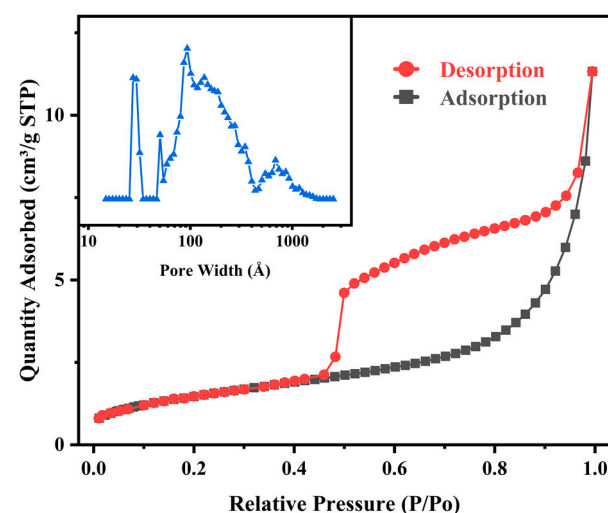


Figure 4. N₂ adsorption–desorption isotherms of the sample T160.

2.2. Surface Elements and Composition

In order to improve the photocatalytic activity of the samples and explore the influence of noble metal deposition on the performance, different noble metals were deposited on the surface of TiO₂ microspheres by photoreduction method, and relevant tests were carried out. The surface chemical composition of bare and metal modified T160 was characterized by XPS analysis, and the related data are shown in Figures 5 and 6 and Table 2. The banding energies for titanium, oxygen, gold, silver copper, palladium,

and platinum were evaluated after deconvolution based on the previous literature regarding XPS analysis [22,24,30,31]. It has been found that titanium exists in the form of Ti^{4+} (Ti 2p_{3/2} at 458.8 eV and Ti 2p_{1/2} at 464.6 eV). Meanwhile, oxygen can be found in two forms, which could be attributed as lattice oxygen (530.0 eV) and vacancy oxygen (531.5 eV). The above results could demonstrate the high purity and clean surface of the samples before photodeposition.

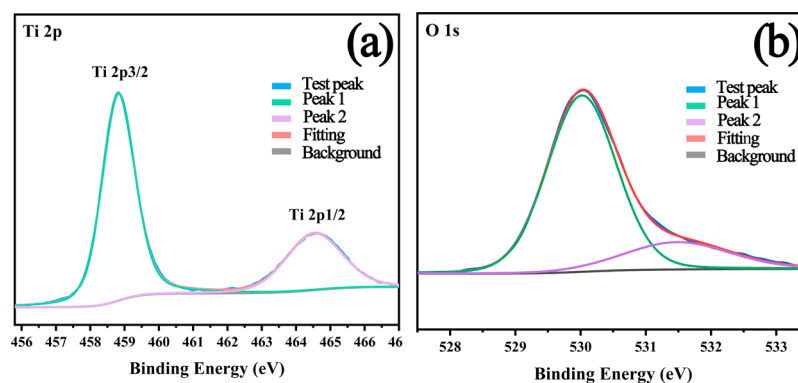


Figure 5. XPS spectra of T160 sample: (a) Ti 2p, (b) O 1s.

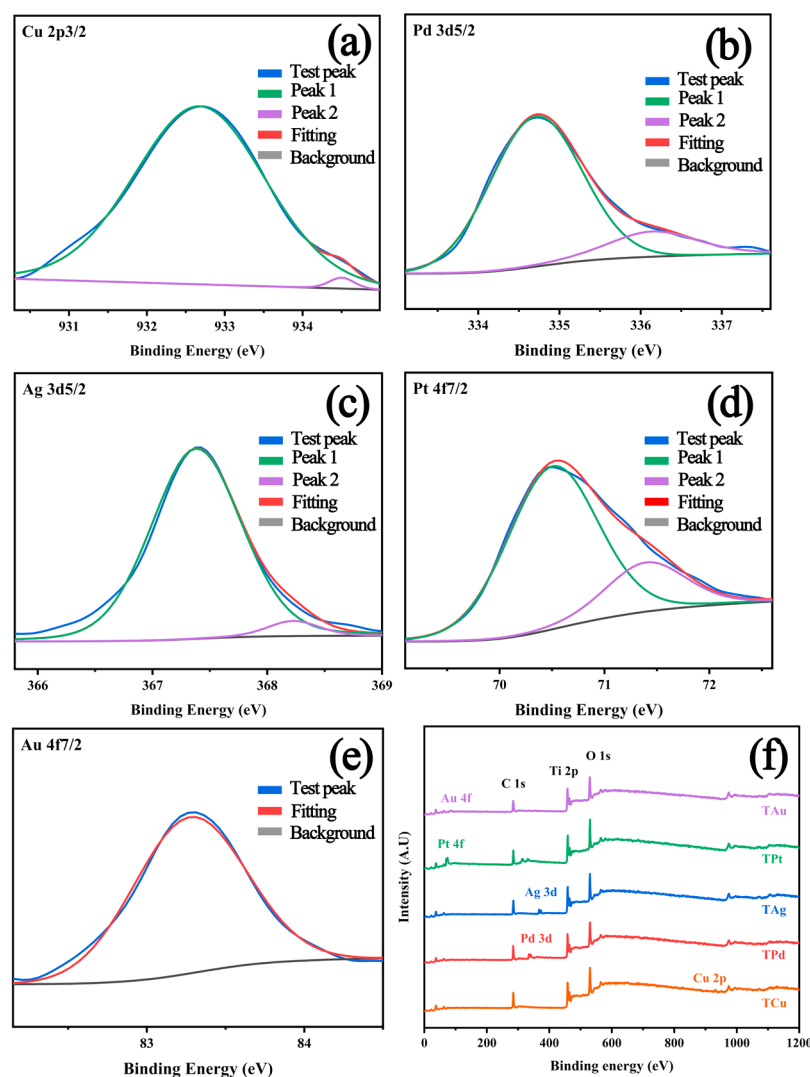


Figure 6. XPS spectra of modified samples: (a) Cu 2p, (b) Pd 3d, (c) Ag 3d, (d) Pt 4f, (e) Au 4f, and (f) full spectra.

Table 2. Surface composition of samples.

Samples		TCu	TPd	TAg	TPt	TAu
Content (at%)	O	63.3	66.7	63.6	65.0	65.7
	Ti	34.5	29.6	34.3	31.2	32.3
	Cu	2.2	-	-	-	-
	Pd	-	3.7	-	-	-
	Ag	-	-	2.1	-	-
	Pt	-	-	-	3.8	-
	Au	-	-	-	-	2.0

As can be seen in Table 2, the proportions of noble metal elements on the surface were all higher than the theoretical value of 2 wt%, indicating that the noble metals were well deposited on the surface of the sample (TPt was chosen as an example to display the morphology of the sample modified by noble metal deposition which can be found in Figure S3). Usually, the proportion of noble metal elements was higher than the theoretical value because only the surface (about several nanometer levels) could be detected by XPS, and the noble metals were deposited on the sample surface.

Copper in the TCu sample could be divided into three valence states by the deconvolution analysis, most of which were Cu⁰ and Cu⁺ (932.7 eV); additionally, there was a small amount of Cu²⁺ (934.5 eV) [31–33]. Two forms of Pd elements existed in the TPD sample, i.e., most of it was Pd⁰ (334.7 eV), and a small part was Pd²⁺ (336.2 eV). Similar to copper, most of the silver existed in the oxidation state as Ag⁺ (367.4 eV), and only a small part existed as zero-valent Ag⁰ (368.2 eV). In the case of platinum, a similar situation was obtained, i.e., zero-valent Pt⁰ (70.5 eV) existed as the main part, and the other part was Pt⁺ (71.4 eV). However, different results were observed for the Au deposition, i.e., all the Au existed as zero-valent Au⁰. Overall, based on the XPS results, it could be found that the noble metals were well deposited on the surface of TiO₂ microspheres by photoreduction. In addition, the proportion of vacant oxygen to the total oxygen element was increased (Table S2), which might be caused by the combination of the noble metal with lattice oxygen and the oxidation of the noble metal.

2.3. Visible and UV Absorption Properties

Without the noble metal modification, there was no visible light absorption for bare T160 as a result of the wide band gap of bare anatase TiO₂. The light absorption ability of all modified samples was significantly enhanced after the modification of noble metal deposition, as shown in Figure 7, and it was also reflected in the macroscopic color of the samples, as shown in Figure S4. At the same time, localized surface plasmon resonance (LSPR) characteristic absorption peaks could be observed obviously, e.g., the LSPR absorption peaks of TAg and TAU samples appeared around 490 nm and 545 nm, respectively, which were similar to the previous literature [34–36]. However, the remaining samples did not exhibit clear LSPR peaks, which may be caused by the different valence states of the surface metals and the shielding effect of the metals themselves [32].

As revealed by UV-Vis diffuse reflectance spectroscopy, the band gap of samples was determined using the following equation:

$$(Ah\nu)^{n/2} = B(h\nu - E_g) \quad (1)$$

where A is the absorption coefficient, $h\nu$ is the light energy, B is a constant, E_g is the optical bandgap, n is equal to 1 for an indirect bandgap and 4 for a direct bandgap, the E_g is obtained by Tauc-plot. TiO₂ is known as an indirect semiconductor; according to the curve plots in Figure 7 the band gaps were calculated and are shown in Figure 8. After the noble metal deposition, the band gaps of the samples were decreased because the deposition of noble metals would change the energy band structure of the sample surface and lead to the shift of the Fermi level. At the same time, noble metals with different valences can form

surface heterojunctions with the samples to further affect their band gaps [22]. Therefore, the types and valences of noble metals lead to differences in the final band gaps. Among them, the TPt band gap was changed the most, i.e., from 3.16 eV to 1.61 eV.

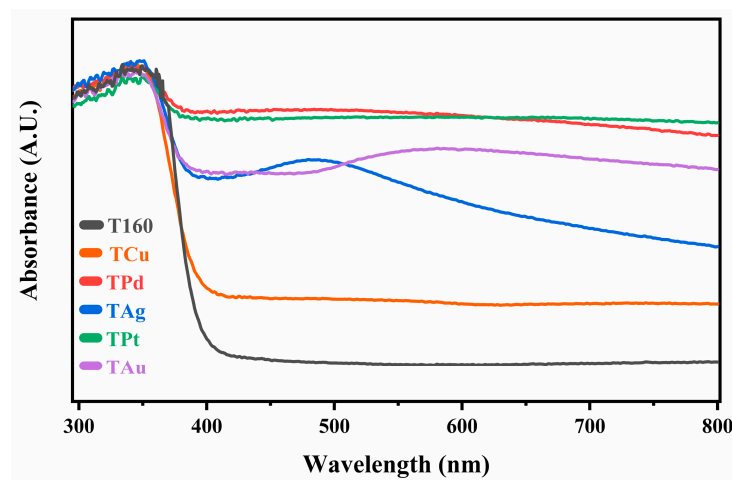


Figure 7. UV-Vis absorption spectra of bare and modified samples.

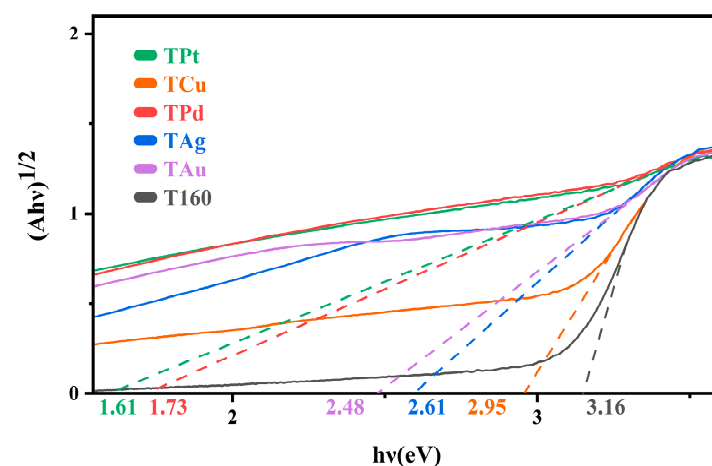


Figure 8. The band gap of the bare and modified samples.

2.4. Evaluation of Photocatalytic Degradation Activity

The photocatalytic activities of different noble metal modified samples on the degradation of TC are shown in Figure 9. The photocatalytic degradation efficiency was improved obviously for all the samples after the noble metal modification. Among all samples, the largest improvement was obtained for the TPt sample, which reached 147% higher than that of the bare T160, and the improvement of the TAg samples was the lowest, which reached only 12% higher than that of T160. It should be pointed out that although the improvement of the photocatalytic activity of the sample was quite similar to the photocatalytic absorption ability, the light absorption characteristics of the samples still could not directly reflect the photocatalytic degradation efficiency, and similar situations have also been reported in previous literature [37]. For example, the TCu sample displayed the smallest increase in light absorption but possessed the second-highest photocatalytic degradation activity among the samples, probably due to the heterojunctions formed by different valences of copper [32,38–40]. Similar to the TCu sample, other samples with multiple valence states (TPd, TPt) also exhibited good photocatalytic activity. In the case of the Ag-modified sample, its poor activity was probably due to the lowest work function of silver and less content of different valence states. In addition, according to the kinetic linear fitting, the degradation efficiency of the TCu sample exhibited a slight decrease with

irradiation time (within 45 min); it may be caused by the instability of Cu with different valences in an acidic solution [41–43].

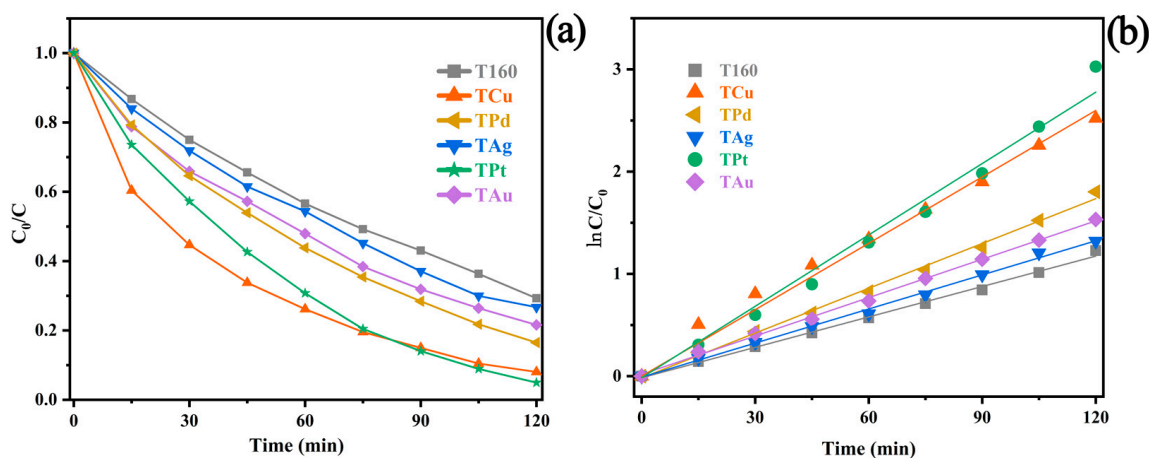


Figure 9. Photocatalytic activity of bare and modified samples: (a) degradation of TC, (b) kinetic linear fitting curves.

2.5. Evaluation of Photocatalytic Hydrogen Generation Activity

The photocatalytic activity of hydrogen generation of the samples deposited with different noble metals is shown in Figure 10. Similar to the photocatalytic degradation of TC, the deposition of noble metals could obviously enhance the photocatalytic activity on hydrogen generation for all the samples, especially for the TPt sample. Based on the experimental results, it could be found that the TPt sample exhibited the largest hydrogen generation rate, and the TAg sample had the lowest hydrogen production efficiency. Interestingly, the photocatalytic hydrogen generation rates were consistent with the work function of those modified noble metals (the values of the work function/eV: Pt > Pd > Au > Cu > Ag) [44–46]. Since photocatalytic hydrogen generation is a reduction reaction, the work function of the noble metal determined the direct utilization of photogenerated electrons. Therefore, the work function of noble metals was the key factor and had the most influence on the reaction rate, while the heterojunction of different valence states and particle size of the noble metal (Figure S6) could also make a contribution. Meanwhile, the higher content of Pt (Table 3) compared to other noble metals might also be the reason; otherwise, for the TPt and TPd, those samples had similar content of noble metals but showed significant differences in activity. This phenomenon further verifies our inference about the effect of the work function of noble metals on photocatalytic activity.

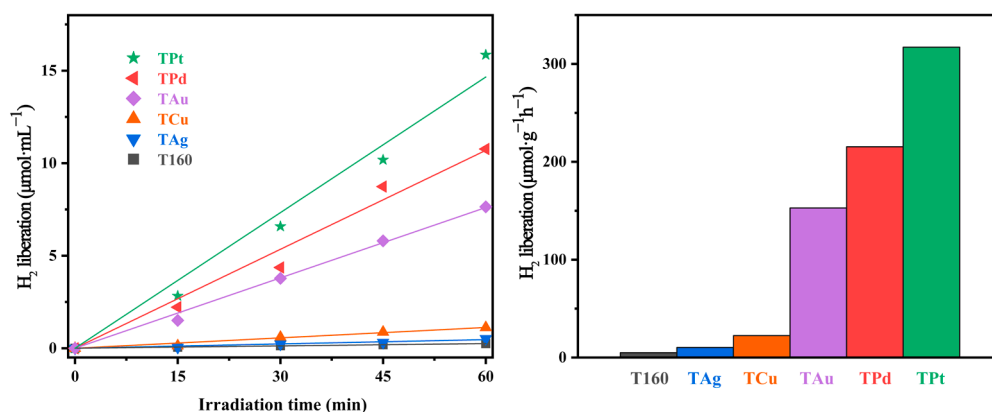


Figure 10. The photocatalytic hydrogen generation of bare and modified samples.

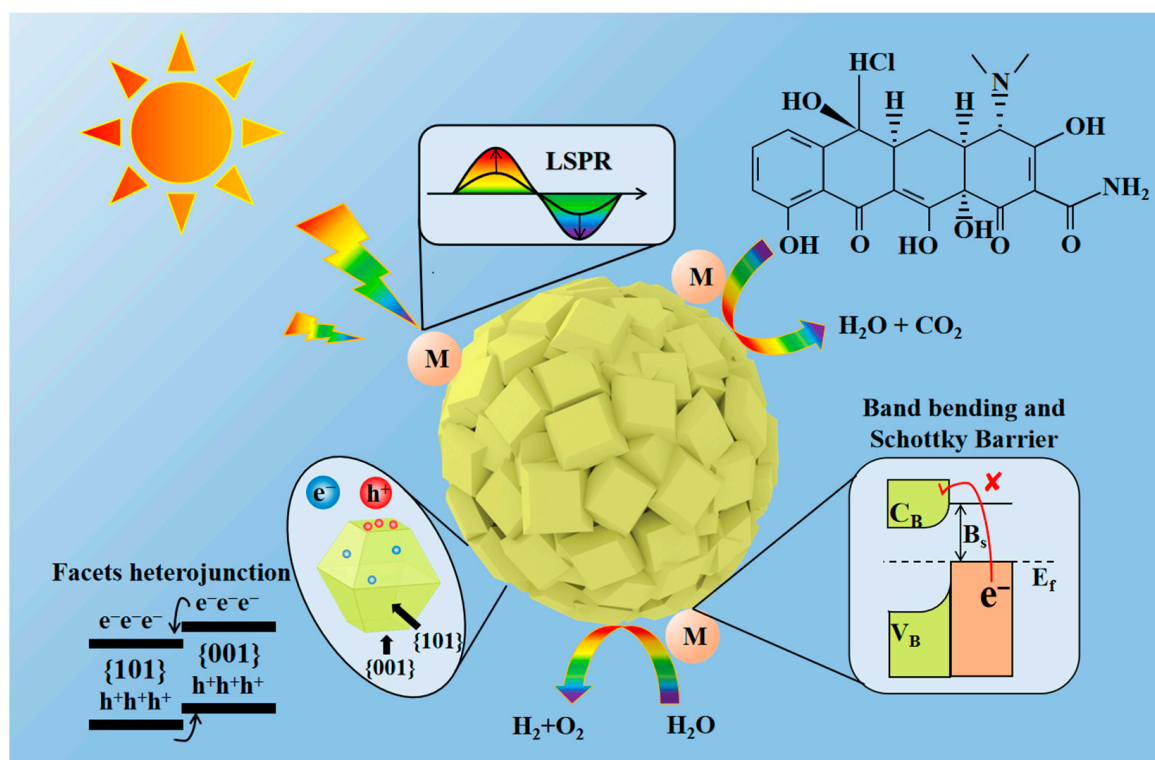
Table 3. The photocatalytic degradation efficiency of the bare and modified samples.

Samples	Degradation Rate in 2 h (%)	Increase Rate Compared with T160 (%)	K (Kinetic Linear Fitting)	R (k/k160)
T160	70.71	0.00	0.00991	1.00
TCu	91.96	21.25	0.02008	2.03
TPd	83.50	12.79	0.01461	1.47
TAg	73.28	2.57	0.01111	1.12
TPt	95.06	24.35	0.02450	2.47
TAu	78.40	7.69	0.01251	1.26

Additionally, platinum preferred to be deposited on the {101} facet during the photodeposition (Figure S3). Photogenerated electrons were easily aggregated on the {101} facets due to crystalline facet heterojunctions, while platinum could further enrich electrons to form electron traps, which were beneficial for H₂ generation. Overall, the highest photocatalytic activity of the TPt sample on H₂ production was caused by the combination of the above factors together.

2.6. Photocatalytic Reaction Mechanism

To further understand the influence of morphology, composition, and structure on material properties, the photocatalytic mechanism was investigated for the noble metal modified co-exposed {001} and {101} faceted TiO₂ hierarchically structured microspheres (as shown in Figure 11 and Figure S7). The light absorption was enhanced obviously by the LSPR effect [34–36] when the noble metal was deposited on the sample surface.

**Figure 11.** Schematic diagram of the proposed photocatalytic mechanism.

The photocatalytic reaction processes can be briefly introduced as four steps, i.e., photoexcitation, charged carrier separation, surface reaction, and recombination. At first, the electron-hole pairs were generated by the photoirradiation since the energy of the irradiation source was higher than the intrinsic band gap of TiO₂, then the electron-hole pairs were spontaneously separated under the crystal facet effect, and negative electrons and positive holes migrated to the {101} and {001} crystal facets [10,24],

respectively. Meanwhile, the surface-deposited noble metal, acting as an electron trap, changed the Fermi level, further promoting the separation of electron-hole pairs [22,27]. Therefore, the separated electrons and holes would migrate to the surface of microspheres and carry out oxidation (photocatalytic degradation) and reduction reactions (photocatalytic hydrogen production) under light irradiation. Of course, parts of the electrons and holes were recombined during the photocatalytic reaction processes and thus could decrease the photocatalytic efficiency, and how to decrease or delay the recombination is still a hot topic in the photocatalysis area.

3. Materials and Methods

3.1. Synthesis of Materials

The chemical reagents during the synthesis process, purchased from Aladdin company, were used without further treatment in this study. Sodium hexafluorotitanate (Na_2TiF_6 , Shanghai, Macklin Inc. China; Macklin Inc.; purity $\geq 98\%$) was used as the Ti source, while the F ion was used to control the morphology of the obtained TiO_2 microspheres. In a typical procedure, 0.15588 g (0.75 mmol) Na_2TiF_6 and 60 mL deionized water were mixed in a 100 mL Teflon-lined autoclave at room temperature. After ultrasonic treatment for 0.5 h, an autoclave (100 mL Teflon-lined) was kept at different temperatures (i.e., 100 °C, 120 °C, 140 °C, 160 °C, 180 °C, and 200 °C) for 6 h, then cooled to room temperature naturally. The obtained white precipitate was collected centrifugally and washed with deionized water, and the centrifuge/washing process was repeated three times to remove any residual inorganic ions. Finally, the TiO_2 microsphere powder was collected by freeze-drying at -85 °C for 24 h. The obtained samples at different temperatures were named accordingly as T100 (100 °C), T120 (120 °C), T140 (140 °C), T160 (160 °C), T180 (180 °C) and T200 (200 °C), respectively.

For the surface modification, $\text{H}_2\text{PtCl}_6 \cdot 6\text{H}_2\text{O}$, $\text{HAuCl}_4 \cdot 3\text{H}_2\text{O}$, AgNO_3 , $\text{CuSO}_4 \cdot 5\text{H}_2\text{O}$, and K_2PdCl_6 were used as noble metals sources. In a typical procedure, 0.5 g of T160 was ultrasonically dispersed in a glass tube containing a mixed solution with 12.5 mL methanol and 12.5 mL deionized water. Then, related noble metal salt solutions were added (2 wt% of noble metal with respect to TiO_2). Afterwards, the glass tube was covered with a latex stopper, and argon gas was purged through a plastic tubule placed at the bottom of the tube for 15 min to remove the air by Ar bubbling. Then, the tube was sealed and irradiated with a mercury lamp (300 W, 10 cm distance from the lamp), and the suspension was continuously stirred during 1 h irradiation. Finally, the powder was collected and washed with deionized water three times. After freeze-drying at -85 °C for 24 h, the samples modified by different noble metals were labeled as TCu (Cu modified), TPd (Pd modified), TAg (Ag modified), TPt (Pt modified), and TAU (Au modified).

3.2. Characterization of Materials

X-ray diffraction patterns of the powders were recorded on an X-ray diffractometer (XRD, PANalytical Empyrean X-ray diffractometer, PANalytical, Etten Leur, Netherlands) equipped with a Cu $K\alpha$ radiation ($\lambda = 0.15418$ nm) source. The accelerating voltage and the applied current were 40 kV and 40 mA; the step size was 0.2° . The diffraction data were obtained over the range $10^\circ \leq 2\theta \leq 90^\circ$ ($5^\circ/\text{min}$). The morphologies of the powders were analyzed by field-emission scanning electron microscopy (SEM, SU8010, Hitachi Limited Company, Tokyo, Japan) operating with deceleration mode at 1 kV accelerating voltage and 10 mA applied current. Surface areas and porosities of the samples were characterized using nitrogen sorption measurements conducted at 77 K, and the Brunauer–Emmett–Teller (BET) method was used to analyze the specific surface area (BET, ASAP 2020 PLUS, Micromeritics, America). The surface properties (chemical composition and state of elements) were evaluated by X-ray photoelectron spectroscopy (XPS, PHI5000, ULVAC-PHI Inc., Chigasaki, Japan) with C 1s (284.8 eV) as a reference for binding energy. The photoabsorption features were estimated by UV-Vis diffuse reflectance spectroscopy (DRS,

UV3600, Shimadzu Corporation, Kyoto, Japan). A laser particle size analyzer (LPS, MS 2000, Malvern, Malvern, UK) was employed to characterize the size distribution of products.

3.3. Photocatalytic Activity Evaluation

The photocatalytic activity of the samples was evaluated by decolorization of tetracycline hydrochloride (TC) aqueous solutions at room temperature. Typically, 0.03 g of the as-prepared TiO₂ powder was dispersed in 100 mL of 10 mg/L TC aqueous solution in a photocatalytic reactor. Prior to irradiation, the suspension was magnetically stirred in dark conditions for 30 min to reach an adsorption/desorption equilibrium. Then the suspension was kept stirring and irradiated for different durations under a xenon lamp (300 W, 100 mW/cm²) at a working distance of 10 cm (circulating water cooling). After every 15 min of photoirradiation, 6 mL aliquot was sampled (medical disposable syringe; 10 mL) and centrifuged (8000 rpm, room temperature) to remove the particles, and the TC concentration was analyzed by measuring the absorption intensity using a UV-1800 UV-Vis spectrophotometer (UV-Vis spectrophotometer, UV-1800, Shanghai, Macy, China). The degradation rate of TC is expressed by the following formula:

$$D_t = \frac{C_0 - C_t}{C_0}, \quad (2)$$

where D_t was the degradation rate, C_0 was the concentration after adsorption/desorption equilibrium, and C_t was the concentration at the duration of t .

For hydrogen generation, methanol was used as the sacrificial agent, and a test tube (25 mL) was used for the hydrogen generation reaction. Typically, 0.05 g of the as-prepared TiO₂ microsphere was dispersed in 5 mL aqueous solution of methanol (50 vol%). After bubbling argon gas (15 min), the tube was sealed and placed in the hydrogen production system. A trace gas sampling needle (100 μ L) was used for sampling every 15 min during the reaction. The extractive gas sample, including produced hydrogen, was passed into a gas chromatograph (gas chromatograph, GC-9790 Plus, FULI Instruments, Wenling, China), and then the amount of produced hydrogen during the reaction could be detected and calculated.

4. Conclusions

In summary, TiO₂ hierarchical microspheres with co-exposed {001} and {101} faceted were prepared by one-step hydrothermal method at 160 °C for 6 h, and the as-obtained sample possessed excellent monodispersity and crystallinity. The photocatalytic activities of the microspheres on TC degradation and hydrogen generation were enhanced obviously by surface noble metal modification, especially the microspheres modified with Pt exhibited the highest photocatalytic activities on both of TC degradation (the TPt sample showed the largest improvement, i.e., the activity reached 1.47 times higher than that of bare T160) and hydrogen production (the largest improvement was also observed for the TPt sample, i.e., the activity was more than 30 times as the bare T160, reaching more than 300 μ mol·g⁻¹·h⁻¹), probably because of the Pt was selectively deposited on the {101} crystal facet which could enhance the crystal facet heterojunction effect and its larger work function. The synergy of co-exposed {001}/{101} crystal facets with noble metals was proposed, which could provide valuable suggestions for the design and development of highly active photocatalysts.

Supplementary Materials: The following supporting information can be downloaded at: <https://www.mdpi.com/article/10.3390/catal13060995/s1>, Figure S1: Raman spectroscopy of T160; Figure S2: Low magnification SEM image of T160; Figure S3: SEM image of TPt; Figure S4: Macroscopic color of the samples; Figure S5: The change of absorption spectrum during the TC degradation (TPt); Figure S6: SEM image of deposited samples, (a) TCu, (b) TPd, (c) TAG, (d) TPt, (e) TAU; Figure S7: Schematic diagram of photogenerated electron transfer and electron trap of noble-metal; Table S1: Crystallite sizes of samples calculated from XRD by Debye-Scherrer Formula; Table S2: The content of vacancy oxygen (Ov); Table S3: The Photocatalytic activity of the samples and P25.

Author Contributions: Conceptualization, Z.W. and Y.C.; methodology, Z.W. and Y.C.; investigation, H.H., J.W. and Y.X.; resources, Z.W. and Y.C.; writing—original draft preparation, H.H. and Q.K.; writing—review and editing, H.H., Z.W. and Y.C.; visualization, H.H.; supervision, Z.W. and Y.C.; funding acquisition, Z.W. and Y.C. All authors have read and agreed to the published version of the manuscript.

Funding: This work was supported by the National Natural Science Foundation of China (NSFC) (51802087 and 51004046), the Natural Science Foundation of the Hubei province of China (2019CFB524 and 2010CDB05806), and the Green Industry Leading Program of Hubei University of Technology (XJ2021002101).

Data Availability Statement: Not applicable.

Conflicts of Interest: The authors declare no conflict of interest.

References

1. Xin, Y.; Zhu, Q.; Gao, T.; Li, X.; Zhang, W.; Wang, H.; Ji, D.; Huang, Y.; Padervand, M.; Yu, F.; et al. Photocatalytic NO removal over defective Bi/BiOBr nanoflowers: The inhibition of toxic NO₂ intermediate via high humidity. *Appl. Catal. B Environ.* **2023**, *324*, 122238. [CrossRef]
2. Padervand, M.; Lichtfouse, E.; Robert, D.; Wang, C. Removal of microplastics from the environment. A review. *Environ. Chem. Lett.* **2020**, *18*, 807–828. [CrossRef]
3. Padervand, M.; Asgarpour, F.; Akbari, A.; Sis, B.E.; Lammel, G. Hexagonal Core–Shell SiO₂[–MOYI]Cl–Ag Nanoframeworks for Efficient Photodegradation of the Environmental Pollutants and Pathogenic Bacteria. *J. Inorg. Organomet. Polym.* **2019**, *29*, 1314–1323. [CrossRef]
4. Takami, N.; Harada, Y.; Iwasaki, T.; Hoshina, K.; Yoshida, Y. Micro-size spherical TiO₂(B) secondary particles as anode materials for high-power and long-life lithium-ion batteries. *J. Power Sources* **2015**, *273*, 923–930. [CrossRef]
5. Zhang, W.; He, H.L.; Tian, Y.; Lan, K.; Liu, Q.; Wang, C.Y.; Liu, Y.; Elzatahry, A.; Che, R.C.; Li, W.; et al. Synthesis of uniform ordered mesoporous TiO₂ microspheres with controllable phase junctions for efficient solar water splitting. *Chem. Sci.* **2019**, *10*, 1664–1670. [CrossRef]
6. Ding, Y.; Zhang, T.T.; Liu, C.; Yang, Y.; Pan, J.H.; Yao, J.X.; Hu, L.H.; Dai, S.Y. Shape-controlled synthesis of single-crystalline anatase TiO₂ micro/nanoarchitectures for efficient dye-sensitized solar cells. *Sustain. Energy Fuels* **2017**, *1*, 520–528. [CrossRef]
7. Yang, H.G.; Sun, C.H.; Qiao, S.Z.; Zou, J.; Liu, G.; Smith, S.C.; Cheng, H.M.; Lu, G.Q. Anatase TiO₂ single crystals with a large percentage of reactive facets. *Nature* **2008**, *453*, 638–641. [CrossRef] [PubMed]
8. Han, X.G.; Kuang, Q.; Jin, M.S.; Xie, Z.X.; Zheng, L.S. Synthesis of titania nanosheets with a high percentage of exposed (001) facets and related photocatalytic properties. *J. Am. Chem. Soc.* **2009**, *131*, 3152–3153. [CrossRef] [PubMed]
9. Wen, C.Z.; Zhou, J.Z.; Jiang, H.B.; Hu, Q.H.; Qiao, S.Z.; Yang, H.G. Synthesis of micro-sized titanium dioxide nanosheets wholly exposed with high-energy {001} and {100} facets. *Chem. Commun.* **2011**, *47*, 4400–4402. [CrossRef]
10. Yu, J.; Low, J.; Xiao, W.; Zhou, P.; Jaroniec, M. Enhanced photocatalytic CO₂-reduction activity of anatase TiO₂ by coexposed {001} and {101} facets. *J. Am. Chem. Soc.* **2014**, *136*, 8839–8842. [CrossRef]
11. Liu, T.; Zhang, H. Novel Fe-doped anatase TiO₂ nanosheet hierarchical spheres with 94%{001} facets for efficient visible light photodegradation of organic dye. *RSC Adv.* **2013**, *3*, 16255–16258. [CrossRef]
12. Ji, L.; Liu, X.; Xu, T.; Gong, M.; Zhou, S. Preparation and photocatalytic properties of carbon/carbon-doped TiO₂ double-layer hollow microspheres. *J. Sol-Gel Sci. Technol.* **2020**, *93*, 380–390. [CrossRef]
13. Xie, J.; Jiang, D.; Chen, M.; Li, D.; Zhu, J.; Lü, X.; Yan, C. Preparation and characterization of monodisperse Ce-doped TiO₂ microspheres with visible light photocatalytic activity. *Colloids Surf. A Physicochem. Eng. Asp.* **2010**, *372*, 107–114. [CrossRef]
14. Akple, M.S.; Low, J.; Qin, Z.; Wageh, S.; Al-Ghamdi, A.A.; Yu, J.; Liu, S. Nitrogen-doped TiO₂ microspheres with enhanced visible light photocatalytic activity for CO₂ reduction. *Chin. J. Catal.* **2015**, *36*, 2127–2134. [CrossRef]
15. Wang, W.; Liu, Y.; Qu, J.; Chen, Y.; Shao, Z. Nitrogen-doped TiO₂ microspheres with hierarchical micro/nanostructures and rich dual-phase junctions for enhanced photocatalytic activity. *RSC Adv.* **2016**, *6*, 40923–40931. [CrossRef]
16. Park, B.-G. Photocatalytic Activity of TiO₂-Doped Fe, Ag, and Ni with N under Visible Light Irradiation. *Gels* **2021**, *8*, 14. [CrossRef]
17. Hu, K.; Lei, E.; Hu, C.; Zhao, D.; Zhu, M.; Wang, J.; Zhao, W. gC₃N₄/TiO₂ composite microspheres: In situ growth and high visible light catalytic activity. *CrystEngComm* **2020**, *22*, 7104–7112. [CrossRef]
18. Ma, Y.; Zhang, C.; Li, C.; Qin, F.; Wei, L.; Hu, C.; Hu, Q.; Duo, S. Nanoscaled Bi₂O₄ confined in firework-shaped TiO₂ microspheres with enhanced visible light photocatalytic performance. *Colloids Surf. A Physicochem. Eng. Asp.* **2019**, *580*, 123757. [CrossRef]
19. Wang, W.S.; Wang, D.H.; Qu, W.G.; Lu, L.Q.; Xu, A.W. Large ultrathin anatase TiO₂ nanosheets with exposed {001} facets on graphene for enhanced visible light photocatalytic activity. *J. Phys. Chem. C* **2012**, *116*, 19893–19901. [CrossRef]

20. He, H.Y.; Lin, J.H.; Fu, W.; Wang, X.L.; Wang, H.; Zeng, Q.S.; Gu, Q.; Li, Y.M.; Yan, C.; Tay, B.K.; et al. MoS₂/TiO₂ edge-on heterostructure for efficient photocatalytic hydrogen evolution. *Adv. Energy Mater.* **2016**, *6*, 1600464. [[CrossRef](#)]
21. Li, G.; Chen, J.; Wu, S.; Yu, Y.; Li, Y.; Gao, J. The relationship between the mesostructure of WO₃/TiO₂ hollow microsphere and its property. *Surf. Innov.* **2017**, *6*, 37–46. [[CrossRef](#)]
22. Wang, A.; Wu, S.; Dong, J.; Wang, R.; Wang, J.; Zhang, J.; Zhong, S.; Bai, S. Interfacial facet engineering on the Schottky barrier between plasmonic Au and TiO₂ in boosting the photocatalytic CO₂ reduction under ultraviolet and visible light irradiation. *Chem. Eng. J.* **2021**, *404*, 127145. [[CrossRef](#)]
23. Wanbayor, R.; Ruangpornvisuti, V. A periodic DFT study on binding of Pd, Pt and Au on the anatase TiO₂(0 0 1) surface and adsorption of CO on the TiO₂ surface-supported Pd, Pt and Au. *Appl. Surf. Sci.* **2012**, *258*, 3298–3301. [[CrossRef](#)]
24. Meng, A.; Zhang, J.; Xu, D.; Cheng, B.; Yu, J. Enhanced photocatalytic H₂-production activity of anatase TiO₂ nanosheet by selectively depositing dual-cocatalysts on {101} and {001} facets. *Appl. Catal. B Environ.* **2016**, *198*, 286–294. [[CrossRef](#)]
25. Shi, Z.; Lin, L.; Chen, R.; Yan, L. Adsorption of CO molecules on anatase TiO₂ (001) loaded with noble metals M (M = Ir/Pd/Pt): A study from DFT calculations. *Mater. Today Commun.* **2021**, *28*, 102699. [[CrossRef](#)]
26. Tong, R.; Liu, C.; Xu, Z.; Kuang, Q.; Xie, Z.; Zheng, L. Efficiently Enhancing Visible Light Photocatalytic Activity of Faceted TiO₂ Nanocrystals by Synergistic Effects of Core-Shell Structured Au@CdS Nanoparticles and Their Selective Deposition. *ACS Appl. Mater. Interfaces* **2016**, *8*, 21326–21333. [[CrossRef](#)]
27. Xiang, Q.; Yu, J.; Jaroniec, M. Tunable photocatalytic selectivity of TiO₂ films consisted of flower-like microspheres with exposed {001} facets. *Chem. Commun.* **2011**, *47*, 4532–4534. [[CrossRef](#)]
28. Han, S.; Niu, Q.; Qin, N.; Gu, X.; Zhang, Y.N.; Hua, G. In situ growth of M-{001} TiO₂/Ti photoelectrodes: Synergetic dominant {001} facets and ratio-optimal surface junctions for the effective oxidation of environmental pollutants. *Chem. Commun.* **2020**, *56*, 1337–1340. [[CrossRef](#)]
29. Chang, Y.; He, P.; Wei, Z.; Chen, Y.; Wang, H.; Wu, C.; Zhou, Z.; Huang, H.; Kowalska, E.; Dong, S. Three-dimensional monodispersed TiO₂ microsphere network formed by a sub-zero sol-gel method. *Mater. Lett.* **2020**, *268*, 127592. [[CrossRef](#)]
30. Feng, N.D.; Lin, H.W.; Song, H.; Yang, L.X.; Tang, D.M.; Deng, F.; Ye, J.H. Efficient and selective photocatalytic CH₄ conversion to CH₃OH with O₂ by controlling overoxidation on TiO₂. *Nat. Commun.* **2021**, *12*, 4652. [[CrossRef](#)]
31. Pham, T.D.; Lee, B.K.; Lee, C.H. The advanced removal of benzene from aerosols by photocatalytic oxidation and adsorption of Cu-TiO₂/PU under visible light irradiation. *Appl. Catal. B Environ.* **2016**, *182*, 172–183. [[CrossRef](#)]
32. Zhu, S.; Chen, X.F.; Li, Z.C.; Ye, X.Y.; Liu, Y.; Chen, Y.; Yang, L.; Chen, M.; Zhang, D.Q.; Li, G.S.; et al. Cooperation between inside and outside of TiO₂: Lattice Cu⁺ accelerates carrier migration to the surface of metal copper for photocatalytic CO₂ reduction. *Appl. Catal. B Environ.* **2020**, *264*, 118515. [[CrossRef](#)]
33. DeSario, P.A.; Gordon, W.O.; Balboa, A.; Pennington, A.M.; Pitman, C.L.; McEntee, M.; Pietron, J.J. Photoenhanced degradation of sarin at Cu/TiO₂ composite aerogels: Roles of bandgap excitation and surface plasmon excitation. *ACS Appl. Mater. Interfaces* **2021**, *13*, 12550–12561. [[CrossRef](#)] [[PubMed](#)]
34. Jung, H.Y.; Yeo, I.S.; Kim, T.U.; Ki, H.C.; Gu, H.B. Surface plasmon resonance effect of silver nanoparticles on a TiO₂ electrode for dye-sensitized solar cells. *Appl. Surf. Sci.* **2018**, *432*, 266–271. [[CrossRef](#)]
35. Tanahashi, I.; Iwagishi, H.; Chang, G. Localized surface plasmon resonance sensing properties of photocatalytically prepared Au/TiO₂ films. *Mater. Lett.* **2008**, *62*, 2714–2716. [[CrossRef](#)]
36. Yao, G.Y.; Liu, Q.L.; Zhao, Z.Y. Studied localized surface plasmon resonance effects of Au nanoparticles on TiO₂ by FDTD simulations. *Catalysts* **2018**, *8*, 236. [[CrossRef](#)]
37. de Brito, J.F.; Tavella, F.; Genovese, C.; Ampelli, C.; Boldrin Zanoni, M.V.; Centi, G.; Perathoner, S. Role of CuO in the modification of the photocatalytic water splitting behavior of TiO₂ nanotube thin films. *Appl. Catal. B Environ.* **2018**, *224*, 136–145. [[CrossRef](#)]
38. Wei, Z.S.; Janczarek, M.; Endo, M.; Wang, K.L.; Balčytis, A.; Nitta, A.; Méndez-Medrano, M.G.; Colbeau-Justin, C.; Juodkakis, S.; Ohtani, B.; et al. Noble metal-modified faceted anatase titania photocatalysts: Octahedron versus decahedron. *Appl. Catal. B Environ.* **2018**, *237*, 574–587. [[CrossRef](#)]
39. Ya, J.; Yang, N.N.; Hu, F.J.; Liu, Z.F.; Lei, E. Preparation and activity evaluation of TiO₂/Cu-TiO₂ composite catalysts. *J. Sol-Gel Sci. Technol.* **2015**, *73*, 322–331. [[CrossRef](#)]
40. Li, Z.H.; Liu, J.W.; Wang, D.J.; Gao, Y.; Shen, J. Cu₂O/Cu/TiO₂ nanotube Ohmic heterojunction arrays with enhanced photocatalytic hydrogen production activity. *Int. J. Hydrogen Energy* **2012**, *37*, 6431–6437. [[CrossRef](#)]
41. Zhen, W.L.; Jiao, W.J.; Wu, Y.Q.; Jing, H.W.; Lu, G.X. The role of a metallic copper interlayer during visible photocatalytic hydrogen generation over a Cu/Cu₂O/Cu/TiO₂ catalyst. *Catal. Sci. Technol.* **2017**, *7*, 5028–5037. [[CrossRef](#)]
42. He, C.; Shu, D.; Su, M.H.; Xia, D.H.; Asi, M.A.; Lin, L.; Xiong, Y. Photocatalytic activity of metal (Pt, Ag, and Cu)-deposited TiO₂ photoelectrodes for degradation of organic pollutants in aqueous solution. *Desalination* **2010**, *253*, 88–93. [[CrossRef](#)]
43. Bai, W.D.; Wu, M.B.; Du, X.L.; Gong, W.L.; Ding, Y.H.; Song, C.H.; Liu, L. Synergistic effect of multiple-phase rGO/CuO/Cu₂O heterostructures for boosting photocatalytic activity and durability. *Appl. Surf. Sci.* **2019**, *40*, 105–113. [[CrossRef](#)]
44. Derry, G.N.; Kern, M.E.; Worth, E.H. Recommended values of clean metal surface work functions. *J. Vac. Sci. Technol. A* **2015**, *33*, 060801. [[CrossRef](#)]

45. Skriver, H.L.; Rosengaard, N.M. Surface energy and work function of elemental metals. *Phys. Rev. B* **1992**, *46*, 7157. [[CrossRef](#)]
46. Hölzl, J.; Schulte, F.K. Work function of metals. In *Solid Surface Physics*; Springer Tracts in Modern Physics; Springer: Berlin/Heidelberg, Germany, 2006; pp. 1–150. [[CrossRef](#)]

Disclaimer/Publisher's Note: The statements, opinions and data contained in all publications are solely those of the individual author(s) and contributor(s) and not of MDPI and/or the editor(s). MDPI and/or the editor(s) disclaim responsibility for any injury to people or property resulting from any ideas, methods, instructions or products referred to in the content.